ORIGINAL ARTICLE

Small calcification indicator in ultrasonography using correlation of echoes with a modified Wiener filter

**Hirofumi Taki · Takuya Sakamoto ·
Makoto Yamakawa · Tsuyoshi Shiina ·
Toru Sato**

Abstract

Purpose The purpose of this study is to improve the calcification depiction ability in ultrasonography using correlation of echoes with a modified Wiener filter.

Methods The waveform of an ultrasound pulse changes when it passes through the location of a calcification. Since the change in echo waveform caused by a calcification decreases the correlation of waveforms in adjacent scan lines, we have proposed a calcification depiction method using the decorrelation of echoes. However, the low signal-to-noise ratio of echoes also decreases the correlation of the echoes. In this study, we employ the correlation of echoes with a modified Wiener filter to suppress the effect of noise, as an indicator of a calcification.

Results The proposed calcification indicator depicted copper cylindrical rods 0.2 mm in size at a depth of 2 cm with a sensitivity of 80% and a positive predictive value of 80%, despite being hardly depicted at all on B-mode ultrasound imaging.

Conclusion This study suggests the potential of the proposed method to improve the performance of calcification depiction by ultrasound devices.

H. Taki (✉) · T. Sakamoto · T. Sato
Graduate School of Informatics, Kyoto University,
Yoshida-honmachi, Sakyo-ku, Kyoto 606-8501, Japan
e-mail: hirofumi.taki@mb6.seikyou.ne.jp

M. Yamakawa
Advanced Biomedical Engineering Research Unit,
Kyoto University, Kyoto, Japan

T. Shiina
Graduate School of Medicine, Kyoto University, Kyoto, Japan

Introduction

In ultrasonographic (US) B-mode imaging, a calcification is characterized by a high-intensity echo region that is associated with posterior acoustic shadowing [1, 2]. However, US has a low sensitivity for calcification detection, resulting in its use as an adjunct to other diagnostic tests. For the evaluation of genitourinary calcifications, X-ray computed tomography (CT) has become the primary imaging modality, relegating US to a secondary role [3]. In renal and abdominal imaging, US has difficulty in detecting small calcifications 3.0 mm or less in size [4]. In the diagnosis of breast cancer, US is used as an adjunct to mammography [5–8]; however, mammography is not effective in young women for detecting calcifications that accompany cancers. Patients with mitral valve leaflet calcification detected on CT are recommended for assessment of mitral valve stenosis by echocardiography [9–12]. For calcification detection without radiation exposure, it is important to improve the performance of US in calcification detection. Improvement in US, in particular, is necessary to realize breast cancer screening for all people including young women.

The echo returned from biological tissue contains the original frequency and its multiples, called harmonic frequencies. Tissue harmonic imaging (THI) is used to improve contrast resolution, as the utilization of harmonic frequencies can suppress multiple scattering artifacts [13–16]. Despite having higher calcification detectability than conventional US devices, THI has a considerably lower sensitivity than CT [3]. In contrast, spatial compound

imaging generates a single B-mode image from multiple sweeps [17–20]. This technique decreases the frame rate and suppresses acoustic shadowing; however, it also improves image quality from the standpoint of mass margins and internal architectures [21]. Therefore, an operator should recognize that the posterior margin of the mass may be better visualized with spatial compound imaging at the cost of helpful features such as acoustic shadowing. In addition, the sensitivity of spatial compound imaging in calcification detection is much lower than that of CT [3]. Another calcification detection strategy is to detect high-intensity echoes in a B-mode image. The constant false alarm rate (CFAR) detector calculates the threshold setting that gives a desired false-alarm probability to extract the position with higher echo intensity than the threshold. The cell averaging (CA) CFAR detector consists of a CFAR detector followed by an additional process that divides the output of each position by the average noise level at the position. The additional process normalizes the echo intensity to compensate for the spatial variation of the mean echo intensity. Because CA CFAR detectors were designed to detect targets while maintaining a constant probability of false alarm [22, 23], they were used for target detection with high-intensity echoes in an inhomogeneous medium [24, 25]. However, the echo intensity from a small calcification is low, and thus small calcification detection is difficult when only selecting high-intensity echo masses. Furthermore, when a layered structure exists immediately behind calcifications, specular echoes from the layered structure interfere with the detection of high-intensity masses originating from calcifications.

The purpose of this study is to propose a useful indicator of calcifications for US under the severe condition that a layered structure exists immediately behind calcifications. Since a small calcification has a low-level blocking effect, the decrease in the echo intensity behind the calcification is obscured. Therefore, most small calcifications are rarely accompanied by acoustic shadowing. However, the waveform of the echo behind a small calcification, being accompanied by no acoustic shadowing, should be altered by the forward scattered wave originating at the calcification. In a recent study, we reported that the waveform change in the echo caused by a calcification will result in decorrelation between adjacent scan lines [26–28]. These reports indicated that the existence of a small calcification was predictable from the waveform difference between adjacent scan lines by calculating the cross-correlation coefficients. Therefore, we proposed a method to indicate small calcifications using the decorrelation between adjacent scan lines [29]. The previous studies employed thin wires to mimic calcifications [28, 29]; however, the characteristics of wires are different from those of mass targets, including calcifications [30]. The smallest calcifications

that mammography can depict are between 0.1 and 0.2 mm [31]. The goal of our study is to approximate the calcification detectability of US to that of mammography. We therefore evaluate the method experimentally using small copper cylindrical rods from 0.1 to 0.3 mm in size. In "Materials and methods", we provide a description of the principle of the calcification indicator, details of the imaging techniques, and the experimental setup. In "Results", we describe the performance of the proposed calcification indicator applied to calcification phantoms. In "Discussion", we investigate the performance of a calcification detection method employing the proposed indicator. Finally, our conclusions are given in "Conclusion".

Materials and methods

The proposed calcification indicator utilizes the decorrelation between adjacent scan lines that is caused by a calcification. We apply this method to adjacent scan lines of in-phase and quadrature (IQ) data. In this section, we briefly explain the principle of the method, and then explain the processes of the method in detail. Finally, we describe the experimental setup.

Principle of the calcification indicator

To detect a calcification, we utilize the decrease in the cross-correlation coefficients between adjacent scan lines, as shown in Fig. 1. The geometric spreading reduces the echo intensity without waveform change. In contrast, creeping waves around the calcification surface, diffraction waves, and multiple reflection waves in the calcification
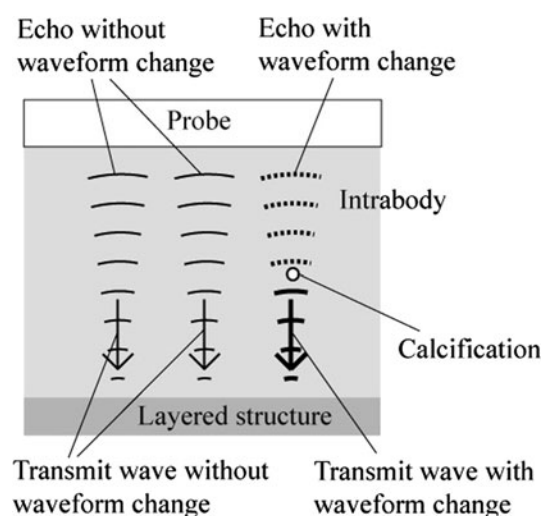

Fig. 1 Waveform change in an ultrasound pulse originating from a calcification, causing a decrease in correlation between adjacent scan lines

occur when an ultrasound pulse passes through the calcification location. It is almost impossible for a calcification to reduce the echo intensity without waveform change. On the other hand, it is probable that the decrease in the echo intensity is inconspicuous while the waveform changes considerably, because of the forward scattered waves that occur at the calcification position, such as diffraction waves. Therefore, the proposed method employing the waveform change caused by a calcification should have a higher sensitivity for the depiction of a calcification than acoustic shadowing, corresponding to the intensity change caused by a calcification.

When a calcification exists in a scan line, the waveform of an ultrasound pulse changes considerably at the calcification location in both the transmit and receive paths because of the occurrence of creeping waves around the calcification surface, diffraction waves, and multiple reflected waves in the calcification. Therefore, the echo waveform of a scan line with a calcification is significantly different from that without a calcification, where the echoes return behind the calcification. This indicates that a decrease in the cross-correlation coefficients can be used to predict the existence of a calcification. Since the proposed method supposes that most of the scatterers in a scan line are also contained in the adjacent scan line, it is obvious that a scan line interval should be much narrower than the beam width [26].

When a small calcification exists close to a layered structure, e.g., a calcification in a mammary duct or on a gallbladder wall, the high-intensity specular echo from the layered structure severely interferes with the depiction of the calcification in a B-mode image. The existence of a layered structure behind a calcification improves the calcification-depiction sensitivity of the proposed method, similar to acoustic shadowing [26]. In this paper, we therefore investigate the performance of the proposed method when a layered structure exists just behind a calcification, which is one of the most difficult cases for the detection of a small calcification with US.

Real data oversampling

Medical acoustic imagers utilize quadrature detectors to acquire IQ data. The detection is equivalent to the multiplication processes between a received signal and two sinusoidal waves, where the phase difference of the two sinusoidal waves is 90° and their center frequency is equal to the transmit center frequency. However, the IQ data correspond with the real and imaginary components of the received signal only at the transmit center frequency. When a broadband signal is employed, the so-called IQ data are actually the oversampled real data with a sampling frequency of four times the transmit center frequency [32]. Acquisition of the raw radio-frequency data is desirable;

however, some medical acoustic imagers store the IQ data. For the broadband signal processing we convert the IQ data to the oversampled real data.

$$g\left(x, z - \frac{\Delta Z}{2}\right) = (-1)^m g_I(x, z), \tag{1}$$

$$g(x, z) = (-1)^m g_Q(x, z), \tag{2}$$

$$z = m\Delta Z, \tag{3}$$

where x and z are the lateral and vertical components, respectively, of a measurement point on a B-mode image, $g(x, z)$ is the oversampled real datum at $P(x, z)$, a pixel in a B-mode image, ΔZ is the range interval, $g_I(x, z)$ and $g_Q(x, z)$ are the in-phase and quadrature components, respectively, of the IQ data at $P(x, z)$, and m is an integer. In this study, the sampling frequency of the IQ data is 15 MHz. Therefore, the sampling frequency of the oversampled RF data is 30 MHz.

Cross-correlation between adjacent scan lines

The proposed indicator of calcifications utilizes the decorrelation of adjacent scan lines. However, the correlation coefficient can be suppressed not only by a calcification but also by noise. When signals cut out by correlation windows have a low signal-to-noise ratio (SNR), the effect of noise on the correlation coefficients is emphasized, interfering with the detection of the decrease in correlation coefficients caused by a calcification. In this study, we employ an echo intensity threshold and a modified Wiener filter to decrease the influence of noise on the cross-correlation coefficients. First, an echo intensity threshold eliminates the signals with low SNR. The proposed method calculates cross-correlations when both the adjacent signals cut out by correlation windows exceed an intensity threshold given by

$$l_t = \alpha n I_0, \tag{4}$$

where α is a positive number, n is the size of the correlation window, and I_0 is the average pixel intensity in a region of interest (ROI).

The cross-correlation coefficient between adjacent scan lines is

$$r\left(x + \frac{\Delta X}{2}, z\right)$$
$$= \max_l \frac{\sum_{z'=z-n\Delta Z}^{z} g(x, z')g(x + \Delta X, z' + l\Delta Z_S)}{\sqrt{\sum_{z'=z-n\Delta Z}^{z} |g(x, z')|^2 \sum_{z'=z-n\Delta Z}^{z} |g(x + \Delta X, z' + l\Delta Z_S)|^2}}, \tag{5}$$

where ΔX is the interval of scan lines, ΔZ_S is the scan interval for the maximization of the correlation coefficient,

and $n\Delta Z$ is the correlation window width. A simple Wiener filter is $S/(S + N)$, where S and N are the expectation of the signal and noise intensity, respectively. Therefore, the cross-correlation coefficient with a simple Wiener filter is expressed as follows:

$$r\left(x + \frac{\Delta X}{2}, z\right)$$
$$= \max_l \frac{\sum_{z'=z-n\Delta Z}^{z} g(x,z')g(x+\Delta X, z'+l\Delta Z_S)}{\sqrt{\sum_{z'=z-n\Delta Z}^{z} |g(x,z')|^2 \sum_{z'=z-n\Delta Z}^{z} |g(x+\Delta X, z'+l\Delta Z_S)|^2} + N},$$

(6)

where we assume that the expectation of the signal intensity is equal to the average echo intensity of two adjacent scan lines. When the noise is dominant, the value of the correlation coefficient with a simple Wiener filter is close to 0; however, this characteristic is unsuitable for the proposed method that depicts the decrease in the cross-correlation coefficient caused by calcifications. Therefore, we employ a modified Wiener filter to suppress the influence of noise on the cross-correlation coefficient according to

$$r\left(x + \frac{\Delta X}{2}, z\right)$$
$$= \max_l \frac{\sum_{z'=z-n\Delta Z}^{z} g(x,z')g(x+\Delta X, z'+l\Delta Z_S) + \beta n I_0}{\sqrt{\sum_{z'=z-n\Delta Z}^{z} |g(x,z')|^2 \sum_{z'=z-n\Delta Z}^{z} |g(x+\Delta X, z'+l\Delta Z_S)|^2} + \beta n I_0},$$

(7)

where ΔX is the interval of scan lines, ΔZ_S is the scan interval for the maximization of the correlation coefficient, $n\Delta Z$ is the correlation window width, and β is a positive number. When the noise is dominant, the indicator expressed by Eq. 7 is close to 1. In this study, the correlation window width was 5 mm including 200 sample points, and we investigate the performance of the proposed method when $\alpha = 1$, 0.5, and 0.25 and $\beta = 0.1$ and 0.01. A transmit beam focused at a calcification depth should emphasize the suppression of correlation caused by the calcification [26]. Therefore, the proposed calcification indicator sets the focus of a transmit beam at the calcification depth. In contrast, the indicator employs dynamic focusing for a receive beam to acquire the same lateral resolution as that of a B-mode image.

Decorrelation of forward scattered waves as an indicator of a calcification

A calcification suppresses the cross-correlation of adjacent scan lines behind it. Therefore, a region with a significantly lower cross-correlation compared with common tissues indicates that a calcification or a target with large acoustic impedance that is a mismatch to soft tissue exists in front of the region. To examine the cross-correlation coefficients of common tissues, we calculate the average, μ, and the standard deviation, σ, of the top 90% of the correlation coefficients in a ROI. The proposed indicator depicts the regions with lower correlation coefficients than $\mu - \gamma\sigma$, where γ is a positive number. In this study, we examined cases in which the correlation threshold parameter $\gamma = 10$, 7.5, and 5, where a larger value of γ indicates a more severe correlation threshold.

The proposed indicator yields a correlation profile from a single B-mode image. This shows that the proposed method involves no decrease in the frame rate when a sufficient signal-processing unit is employed.

Calcification depiction with a totalizing process

The sensitivity of the proposed method for small rods is insufficient for clinical use and largely depends on the parameters α and β. To resolve the two issues, i.e., improvement of the sensitivity of the proposed method and optimization of the parameters α and β, we employ a calcification detection method with a totalizing process [28]. First, the method varies the combination of parameters α and β, where $\alpha = 1$, 0.5 and 0.25 and $\beta = 0.1$ and 0.01. Then, the method totals up all the low correlation regions appearing in the six combinations of parameters α and β.

$$\mathbf{R}_T = \bigcup_{\alpha,\beta} \mathbf{R}_{\alpha\beta},$$

(8)

where $\mathbf{R}_T$ is the totalized low correlation region, and $\mathbf{R}_{\alpha\beta}$ is the low correlation region using a combination of parameters α and β. The method then predicts the existence of calcifications using the totalized low correlation regions.

Experimental setup

Experiments were conducted with a Hitachi EUB-8500 (Hitachi, Tokyo, Japan) US device, which has a function to export raw IQ data. A 7.5-MHz linear array probe was used, where the scan line interval and range interval of the IQ data were 0.13 and 0.05 mm, respectively. Previous studies employed thin wires to mimic calcifications [28, 29]; however, the characteristics of wires are different from those of mass targets, including calcifications [30]. In this study, we prepared a calcification phantom with copper cylindrical rods embedded into a 4% agar gel block, as shown in Fig. 2. We simulated in vivo conditions by placing 1-cm-thick pig skin and subcutaneous fat layer onto the agar gel block. This phantom mimics the gallbladder with calcifications.

Fig. 2 Calcification phantom with a swine skin and subcutaneous fat layer
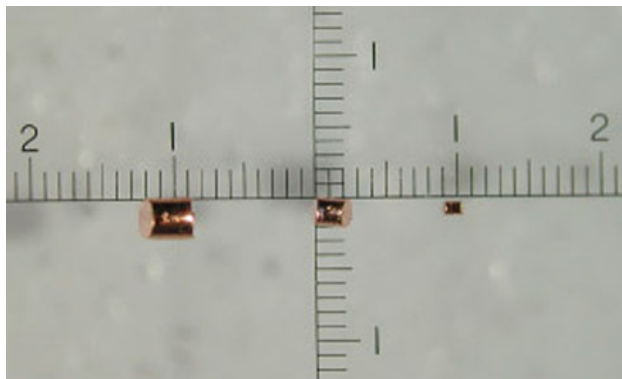

Fig. 3 Copper cylindrical rods used in this study to mimic calcifications and a millimeter scale, where the diameter of each rod is equal to its length. The sizes of the rods are 0.3, 0.2, and 0.1 mm from *left* to *right*

Fig. 4 B-mode image of a calcification phantom **a** with and **b** without a swine fat layer 1 cm thick. *White arrows* indicate copper cylindrical rods embedded at a depth of 2 cm, where the sizes of the rods are 0.3, 0.2, and 0.1 mm from *left* to *right*. The *white broken line* is the boundary of a ROI 1 × 3 cm. The ROI was marked on either side with two stainless spheres 1 mm in diameter

Figure 3 shows a microscopic image of the three kinds of rods used in this study with a millimeter scale. The diameter of each rod is equal to its length, and the sizes of the rods are 0.3, 0.2, and 0.1 mm. Stainless spheres accompanied the copper rods in order to locate them. The agar block contained 1% Tech Polymer particles, spherical polymer particles 7 μm in diameter (Sekisui-Plastics Co., Ltd.). We arranged copper rods and stainless spheres along five lines on a fluororesin sheet 0.1 mm thick, where each line contained three copper rods and two stainless spheres. The sizes of the copper rods arranged along each line were 0.3, 0.2, and 0.1 mm from left to right at 1 cm intervals, and two stainless spheres 1 mm in diameter were set at both sides. Figure 4 shows B-mode images of the
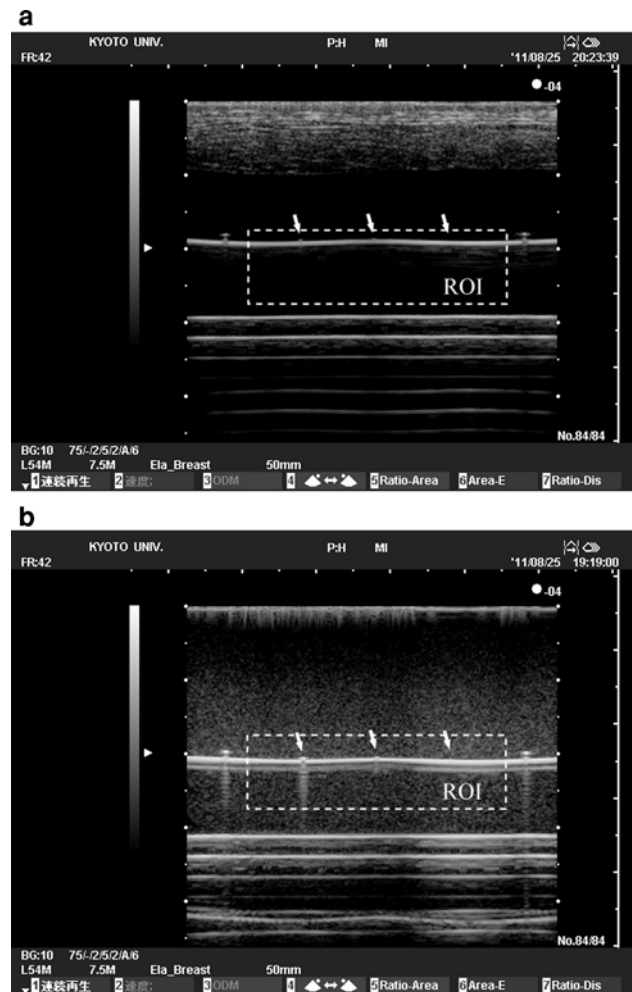
calcification phantom with and without a swine fat layer, where the measurement planes contained one of the five arrangement lines. The size of a ROI was 1 × 3 cm, and each ROI was marked with the two stainless spheres located at both sides of the ROI. In addition, we put the sheet with copper rods and stainless spheres between swine breast tissues, as shown in Fig. 5. This phantom mimics the breast with calcifications. The attenuation of the agar gel with particles was less than 0.1 dB/MHz/cm. In contrast, the attenuation of the swine breast tissue was 3.6 dB/MHz/cm. The large attenuation of the swine breast tissue may be caused by its heterogeneity, which degrades the directivity of the ultrasound beam.

In these setups, specular echoes from the fluororesin sheet had a higher intensity than those from copper rods, indicating that the strategy of selecting high-intensity echo
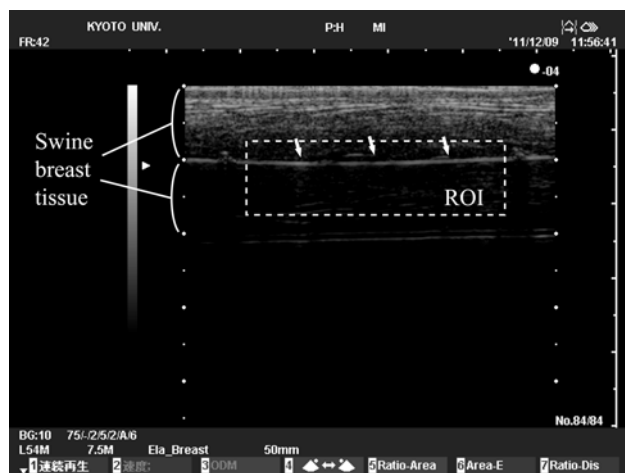
Fig. 5 B-mode image of a calcification phantom that mimics the breast with calcifications. The *white arrows* indicate copper cylindrical rods embedded at a depth of 1 cm, where the sizes of the rods are 0.3, 0.2, and 0.1 mm from *left* to *right*. The *white broken line* is the boundary of a ROI 1 × 3 cm. The ROI was marked on either side with two stainless spheres 1 mm in diameter

masses such as in CA CFAR detectors was unsuitable for small calcification detection. The performance of the proposed method in depicting copper rods of each size and depth was investigated using five IQ data sets of five measurement planes, where each measurement plane contained one of the five arrangement lines on the fluororesin sheet.

The waveform of an ultrasound pulse is changed by a target with large acoustic impedance that is a mismatch to soft tissue. This means that the indicator detects not only copper rods but also small bubbles. Therefore, the calcification phantom should be prepared in such a way as to ensure it contains no bubble, at least in the measurement sections. In addition, all bubbles should be excluded from the boundary between the swine fat layer and the agar gel block.

Results

Figure 6 shows the cross-correlation profiles of two ROIs with and without a swine fat layer, where the size of the ROI is 1 × 3 cm and each ROI contains copper rods 0.3, 0.2, and 0.1 mm in size from left to right, as shown in Fig. 4. The intensity threshold parameter α and the stability parameter β are −6 and −10 dB, respectively. The low correlation regions appear behind the positions of the 0.2 and 0.3 mm rods, and extend along the range direction. The range ambiguity of the proposed indicator is caused by the width of the correlation window. Figure 7 shows the correlation coefficient calculated by the proposed method at a depth of 2 cm and the echo intensity of the layered
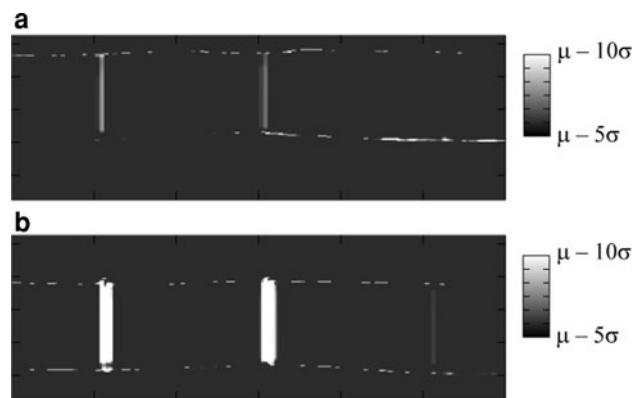

Fig. 6 Normalized cross-correlation profiles of the ROIs **a** with and **b** without the swine fat layer shown in Fig. 4. Each ROI contains three copper rods 0.3, 0.2, and 0.1 mm in size from *left* to *right*. μ and σ are the average and the standard deviation, respectively, of the top 90% of the correlation coefficients in each ROI
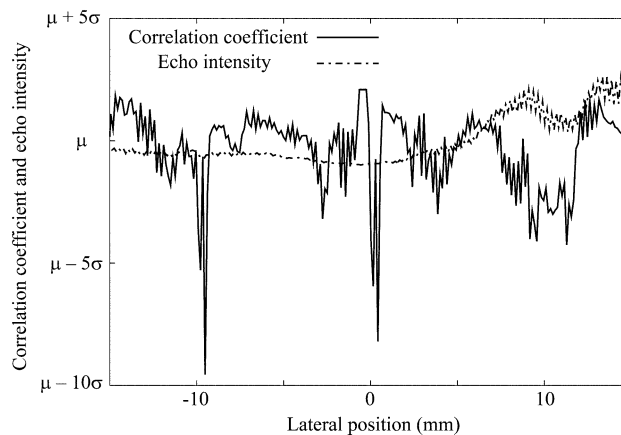

Fig. 7 Correlation coefficient calculated by the proposed method at a depth of 2 cm and echo intensity of the layered structure in the ROI shown in Fig. 4a, where both the correlation coefficient and echo intensity were normalized by their standard deviations. The echo intensity of the layered structure in each scan line was calculated by the maximum of the echo intensity summation for the depth of 0.5 mm, including 10 range samples. Copper rods 0.3, 0.2, and 0.1 mm in size were located at the lateral positions of −10, 0, and 10 mm, respectively

structure in the ROI is shown in Fig. 4a, where both the correlation coefficient and echo intensity were normalized by their standard deviations. The echo intensity of the layered structure in each scan line was calculated by the maximum of the echo intensity summation for the depth of 0.5 mm, including 10 range samples. Copper rods 0.3, 0.2, and 0.1 mm in size were located at the lateral positions of −10, 0, and 10 mm, respectively. The decrease in the echo intensity is less than its standard deviation. In contrast, the correlation coefficient decreases more than eight times its standard deviation at the positions of the 0.3 and 0.2 mm copper rods. This result suggests that the correlation profile is a useful indicator of calcifications and has higher

Table 1 Averages of sensitivities and positive predictive values of the proposed method for the depiction of copper rods; standard deviations are given in *parentheses*

	Copper rod 0.2 mm in size		Copper rod 0.3 mm in size	
	Sensitivity	PPV	Sensitivity	PPV
$\mu - 5\sigma$	0.533 (0.273)	0.850 (0.118)	0.467 (0.207)	0.833 (0.129)
$\mu - 7.5\sigma$	0.200 (0.179)	1 (0)	0.333 (0.103)	1 (0)
$\mu - 10\sigma$	0.133 (0.103)	1 (0)	0.200 (0.179)	1 (0)

Copper rods 0.2 and 0.3 mm in size were embedded in an agar block with a swine fat layer at a depth of 2 cm. We investigated the performance of the proposed indicator using three correlation thresholds: $\mu - 5\sigma$, $\mu - 7.5\sigma$, and $\mu - 10\sigma$. Each indicator employed six combinations of parameters α and β, where $\alpha = 1, 0.5$, and 0.25, and $\beta = 0.1$ and 0.01

Table 2 Sensitivity and positive predictive value of the calcification depiction method with a totalizing process for the detection of copper rods 0.2 and 0.3 mm in size, where the rods were embedded in an agar block with a swine fat layer

	Copper rod 0.2 mm in size		Copper rod 0.3 mm in size	
	Sensitivity	PPV	Sensitivity	PPV
Depth = 2 cm				
$\mu - 5\sigma$	0.8	0.8	0.6	0.75
$\mu - 7.5\sigma$	0.4	1	0.6	1
$\mu - 10\sigma$	0.2	1	0.4	1
Depth = 3 cm				
$\mu - 5\sigma$	0.4	1	0.6	1
$\mu - 7.5\sigma$	–	–	0.4	1
$\mu - 10\sigma$	–	–	0.4	1
Depth = 4 cm				
$\mu - 5\sigma$	–	–	1	0.833
$\mu - 7.5\sigma$	–	–	0.4	1
$\mu - 10\sigma$	–	–	–	–

Table 3 Sensitivity and positive predictive value of the calcification depiction method with a totalizing process for the detection of copper rods 0.2 and 0.3 mm in size, where the rods were embedded in an agar block without a swine fat layer

	Copper rod 0.2 mm in size		Copper rod 0.3 mm in size	
	Sensitivity	PPV	Sensitivity	PPV
Depth = 1 cm				
$\mu - 5\sigma$	0.6	1	1	1
$\mu - 7.5\sigma$	–	–	0.8	1
$\mu - 10\sigma$	–	–	0.6	1
Depth = 2 cm				
$\mu - 5\sigma$	1	1	1	1
$\mu - 7.5\sigma$	1	1	0.8	1
$\mu - 10\sigma$	0.8	1	0.8	1
Depth = 3 cm				
$\mu - 5\sigma$	0.8	1	1	1
$\mu - 7.5\sigma$	0.6	1	1	1
$\mu - 10\sigma$	0.6	1	0.8	1

sensitivity than acoustic shadowing. In the measurement of a calcification phantom without a swine fat layer, a low correlation region appears behind the position of the rod 0.1 mm in size; however, the decrease in correlation caused by the 0.1 mm rod is inconspicuous compared to those caused by the 0.2 and 0.3 mm rods.

To investigate the efficiency of the proposed indicator, we examined the sensitivity and the positive predictive value of a calcification detection method using the calcification indicator, with a sample size of five. The sensitivity is the number of true copper rods depicted by the proposed method over the total number of copper rods embedded in a calcification phantom. The positive predictive value is the number of true copper rods depicted by the proposed method over the number of calcification positions estimated by the proposed method including false images. The correlations between scan lines behind a calcification are suppressed continuously along the range direction. Thus, the calcification detection method predicts that a copper

rod exists in a scan line when the low correlation region continues more than 0.5 times the width of the correlation window along the scan line. We decided that the method was successful in detecting a rod when the method selected a scan line within 1, 0.75, and 0.5 mm from the rod at 4, 3, and 2 cm depth, respectively. Table 1 shows the average and standard deviation of the sensitivities and the positive predictive values of the proposed methods for the detection of copper rods, where three correlation threshold parameters and six combinations of an intensity threshold parameter and a stability constant parameter are employed. Copper rods 0.2 and 0.3 mm in size were embedded in an agar block with a swine fat layer at a depth of 2 cm.

Table 2 shows the sensitivity and the positive predictive value of the calcification detection method with the totalizing process, where the rods were embedded in an agar block with a swine fat layer. In the experiment with a swine fat layer, the proposed calcification detection method with the totalizing process succeeded in detecting 0.2 mm rods

at a depth of 2 cm with a sensitivity of 80% and a positive predictive value of 80%, where $\gamma = 5$ was employed. The positive predictive value of the proposed method employing $\gamma = 7.5$ was improved to 100% at the cost of a decrease in sensitivity to 40%. The proposed method with the totalizing process detected 0.3 mm copper rods at a depth of 2 cm with a sensitivity of 60% and a positive predictive value of 100%, where $\gamma = 7.5$ was employed. No 0.1 mm copper rods were detected by the proposed method.

In the experiment without a swine fat layer, the proposed method with the totalizing process had excellent performance in detecting 0.2 and 0.3 mm copper rods, as shown in Table 3. However, the proposed method detected only a single 0.1 mm copper rod at a depth of 2 cm among 15 0.1 mm copper rods at three depths.

Next, we applied the proposed method to the swine breast tissue including a sheet with copper rods and reference stainless spheres at a depth of 1 cm. The proposed method only depicted 70% of the reference stainless spheres 1 mm in diameter and no copper rods.

Discussion

A previous study depicted thin copper wires from 0.2 to 0.4 mm in diameter [28]. In contrast, the proposed method succeeded in depicting 0.2 mm copper rods embedded in an agar gel with swine tissue, as shown in Table 2. Since the echo intensity returned from a copper wire 0.2 mm in diameter is about 10 times that from a copper rod 0.2 mm in size [30], the calcification detectability of the proposed method in this paper has been improved significantly from that of the previously proposed method.

The severe correlation threshold eliminates false images at the cost of the sensitivity of the method. Since a correlation threshold parameter (γ) of 7.5 eliminated all the false images, setting $\gamma > 7.5$ is inappropriate under the conditions that mimic a gallbladder with calcifications. When the correlation coefficients follow a Gaussian distribution, the correlation coefficients under the thresholds of $\gamma = 5$ and 7.5 account for 2.87×10^{-5} and 3×10^{-12}%, respectively. Because the ROI used in this study consisted of 45,400 measurement points, no false-positive point occurred in the probability of 98.7 and 100% in each image when $\gamma = 5$ and 7.5 were employed, respectively. This investigation supports the result that $\gamma = 7.5$ eliminated all the false images.

The best γ may be between 5 and 7.5. Future work should include the optimization of γ; however, the proposed method is not sensitive to γ and works robustly. Therefore, it is recommended that an operator first employs a low correlation threshold to select all calcification candidates and then judges the candidates using a high correlation threshold. An implementation of the proposed method on an US device is to present the low cross-correlation regions calculated by the proposed method on a B-mode image.

The result shown in Tables 2 and 3 indicates that the attenuation of the signal caused by the swine tissue deteriorates the performance of the proposed method. However, the result using the swine breast tissue with copper rods shows that the performance of the proposed method deteriorates severely when the layered structure is located just behind the heterogeneous medium. One of the reasons for this is the decrease in the correlation between adjacent scan lines. In this study, we set the focal range of the ultrasound beam at the depth of the layered structure. The heterogeneous tissue at the focal range may therefore suppress the cross-correlation between adjacent scan lines. This study shows that the detection of calcifications in the breast needs to be modified for the proposed method, including the optimization of the focal range and correlation window width.

Conclusion

In this study, we investigated the performance of a small calcification indicator for US. A calcification detection method employing the proposed indicator successfully detected copper cylindrical rods 0.2 mm in size at a 2 cm depth with a sensitivity of 80% and a positive predictive value of 80%, despite being hardly depicted at all on B-mode ultrasound imaging. This study suggests the potential of the proposed method to improve the performance of US devices for the detection of calcifications in the gallbladder. The proposed method detected 0.1 mm copper rods with a sensitivity of 7% under ideal conditions without a swine fat layer. However, the proposed method is unsuitable for detecting calcifications in the breast.

The combination of the proposed method with other techniques, e.g., acoustic shadowing, may improve the performance of US in calcification depiction. Therefore, future work should include investigation of a combination of the proposed method with other techniques, and modification of the proposed method to detect calcifications in the breast.

References

1. Janetschek G, Putz A, Feichtinger H. Renal transitional cell carcinoma mimicking stone echoes. J Ultrasound Med. 1988;7:83–6.

2. Roesel GC, Toepfer NJ, Battino BS, Bell TE. A calcified papillary renal cell carcinoma masquerading as a renal pelvic calculus. Curr Urol. 2008;1:217–8.
3. Özdemir H, Demir MK, Temizöz O, et al. Phase inversion harmonic imaging improves assessment of renal calculi: a comparison with fundamental gray-scale sonography. J Clin Ultrasound. 2008;36:16–9.
4. Fowler KAB, Locken JA, Duchesne JH, et al. US for detecting renal calculi with nonenhanced CT as a reference standard. Radiology. 2002;222:109–13.
5. Lamb PM, Perry NM, Vinnicombe SJ, et al. Correlation between ultrasound characteristics, mammographic findings and histological grade in patients with invasive ductal carcinoma of the breast. Clin Radiol. 2000;55:40–4.
6. Jacob D, Brombart JC, Muller C, et al. Analysis of the results of 137 subclinical breast lesions excisions. Value of ultrasonography in the early diagnosis of breast cancer. J Gynecol Obstet Biol Reprod (Paris). 1997;26:27–31.
7. Jackson VP, Reynolds HE, Hawes DR. Sonography of the breast. Semin Ultrasound CT MRI. 1996;17:460–75.
8. Tohno E, Cosgrove DO, Sloane JP. Ultrasound diagnosis of breast diseases. Edinburg: Elsevier Health Sciences; 1994.
9. Mahnken AH, Mühlenbruch G, Das M, et al. MDCT detection of mitral valve calcification: prevalence and clinical relevance compared with echocardiography. AJR Am J Roentgenol. 2007;188:1264–9.
10. Liu F, Coursey CA, Grahame-Clarke C, et al. Aortic valve calcification as an incidental finding at CT of the elderly: severity and location as predictors of aortic stenosis. AJR Am J Roentgenol. 2006;186:342–9.
11. Koos R, Mahnken AH, Sinha AM, et al. Aortic valve calcification as a marker for aortic stenosis severity: assessment on 16-MDCT. AJR Am J Roentgenol. 2004;183:1813–8.
12. Morgan-Hughes GJ, Owens PE, Roobottom CA, et al. Three-dimensional volume quantification of aortic valve calcification using multislice computed tomography. Heart. 2003;89:1191–4.
13. Schmidt T, Hohl C, Haage P, et al. Diagnostic accuracy of phase-inversion tissue harmonic imaging versus fundamental B-mode sonography in the evaluation of focal lesions of the kidney. AJR Am J Roentgenol. 2003;180:1639–47.
14. Rosenthal SJ, Jones PH, Wetzel LH. Phase inversion tissue harmonic sonographic imaging: a clinical utility study. AJR Am J Roentgenol. 2001;176:1393–8.
15. Szopinski KT, Pajk AM, Wysocki M, et al. Tissue harmonic imaging: utility in breast sonography. J Ultrasound Med. 2003;22:479–87.
16. Rosen EL, Soo MS. Tissue harmonic imaging sonography of breast lesions improved margin analysis, conspicuity, and image quality compared to conventional ultrasound. Clin Imaging. 2001;25:379–84.
17. Krücker JF, Meyer CR, LeCarpentier GL, et al. 3D spatial compounding of ultrasound imaging using image-based nonrigid registration. Ultrasound Med Biol. 2000;26:1475–88.
18. Moskalik A, Carson PL, Meyer CR, et al. Registration of 3-dimensional compound ultrasound scans of the breast for refraction and motion correction. Ultrasound Med Biol. 1995;21:769–78.
19. Rohling RN, Gee AH, Berman L. Automatic registration of 3-D ultrasound images. Ultrasound Med Biol. 1998;24:841–54.
20. Huber S, Wagner M, Medl M, et al. Real time spatial compound imaging in breast ultrasound. Ultrasound Med Biol. 2002;28:155–63.
21. Weinstein SP, Conant EF, Sehgal C. Technical advances in breast ultrasound imaging. Semin Ultrasound CT MRI. 2006;27:273–83.
22. Finn HM, Johnson RS. Adaptive detection mode with threshold control as a function of spatially sampled clutter-level estimates. RCA Rev. 1968;29:414–65.
23. Hansen VG, Ward HR. Detection performance of the cell averaging LOG/CFAR receiver. IEEE Trans Aerosp Electron Syst. 1972;5:648–52.
24. Zhu Y, Weight JP. Ultrasonic nondestructive evaluation of highly scattering materials using adaptive filtering and detection. IEEE Trans Ultrason Ferroelectr Freq Control. 1994;41:26–33.
25. Kamiyama N, Okamura Y, Kakee A, et al. Investigation of ultrasound image processing to improve perceptibility of microcalcifications. J Med Ultrason. 2008;35:97–105.
26. Taki H, Sakamoto T, Yamakawa M, et al. Calculus detection for medical acoustic imaging using cross-correlation: simulation study. J Med Ultrason. 2010;37:129–35.
27. Taki H, Sakamoto T, Yamakawa M, et al. Small calculus detection for medical acoustic imaging using cross-correlation between echo signals. Proc IEEE Int Ultrason Symp. 2009;2398–401.
28. Taki H, Sakamoto T, Yamakawa M, et al. Small calcification depiction in ultrasound B-mode images using decorrelation of echoes caused by forward scattered waves. J Med Ultrason. 2011;38:73–80.
29. Taki H, Sakamoto T, Yamakawa M, et al. Indicator of small calcification detection in ultrasonography using decorrelation of forward scattered waves. Proc Int Conf Comput Electr Syst Sci Eng. 2010;175–9.
30. Taki H, Sakamoto T, Yamakawa M, et al. Ultrasound phantom using thin wires for the depiction of calcification—comparison of cross-sections of wire targets and mass targets. IEEJ Trans Electr Inf Syst. 2011;131:1528–34.
31. Manzano-Lizcano JA, Sánchez-Ávila C, Moyano-Pérez L. A microcalcification detection system for digital mammography using the contourlet transform. Adv Comput Exp Eng Sci. 2004;611–6.
32. Taki H, Taki K, Sakamoto, T et al. High range resolution medical acoustic vascular imaging with frequency domain interferometry. Proc IEEE Eng Med Biol Soc. 2010;5298–301.